Spatial dynamics in a predator-prey model with Beddington-DeAngelis functional response

Xiao-Chong Zhang,* Gui-Quan Sun,† and Zhen Jin‡
Department of Mathematics, North University of China, Taiyuan, Shan'xi 030051, People's Republic of China
(Received 3 November 2011; revised manuscript received 31 December 2011; published 28 February 2012)

In this paper spatial dynamics of the Beddington-DeAngelis predator-prey model is investigated. We analyze the linear stability and obtain the condition of Turing instability of this model. Moreover, we deduce the amplitude equations and determine the stability of different patterns. In Turing space, we found that this model has coexistence of H_0 hexagon patterns and stripe patterns, H_π hexagon patterns, and H_0 hexagon patterns. To better describe the real ecosystem, we consider the ecosystem as an open system and take the environmental noise into account. It is found that noise can decrease the number of the patterns and make the patterns more regular. What is more, noise can induce two kinds of typical pattern transitions. One is from the H_π hexagon patterns to the regular stripe patterns, and the other is from the coexistence of H_0 hexagon patterns and stripe patterns to the regular stripe patterns. The obtained results enrich the finding in the Beddington-DeAngelis predator-prey model well.

DOI: 10.1103/PhysRevE.85.021924 PACS number(s): 87.23.Cc, 89.75.Kd, 89.75.Fb, 47.54.−r

I. INTRODUCTION

The Beddington-DeAngelis functional response was introduced by Beddington [1] and DeAngelis *et al*. [2]. It is similar to the well-known Holling-type functional response, but it contains an extra term describing mutual interference by predators. Some biologists have argued that in many cases, especially when predators have to search for food and consequently have to share or compete for food, the functional response in a predator-prey model should be predator dependent. Specifically, Skalski and Gilliam [3] claimed that the predator-dependent functional response can provide better descriptions of predator feeding over a range of predator-prey abundances by comparing the statistical evidence from 19 predator-prey systems with the three predator-dependent functional responses (Hassell-Varley [4], Beddington-DeAngelis [1,2], and Crowley-Martin [5]), and in some cases the Beddington-DeAngelis functional response preformed even better. This model represents most of the qualitative features of the ratio-dependent models but avoids the "low densities problem," which is usually the source of controversy.

The study of pattern formation in reaction-diffusion (RD) systems is a very active research area. Since Turing [6] first proposed RD theory to describe the range of spatial patterns observed in the developing embryo, RD models have been studied extensively to explain patterns in fish skin, mammalian coat markings, phyllotaxis, predator-prey systems, terrestrial vegetation, plankton, intertidal communities, and so on (see Refs. [7–16]). Segel and Jackson [17] were the first to call attention to the fact that Turing's ideas would also be applicable in population dynamics. At the same time, Gierer and Meinhardt [18] gave a biologically justified formulation of a Turing model and studied its properties by employing numerical simulation. Levin and Segel [19] suggested this scenario of spatial pattern formation as a possible origin of planktonic patchiness. In recent years there has been considerable interest in spatial and temporal behavior of interacting species in ecosystems. The dynamical behavior between predator and prey has long been and will continue to be one of the dominant themes in ecosystems due to its universal existence and importance [20–25]. Unfortunately most of the studies about the spatiotemporal predator-prey system with functional response focus on the bifurcation phenomena by varying the control parameter(s), and little attention has been paid to study of the selection of the Turing patterns.

Owing to the insightful work of many scientists over recent years, we can now focus on pattern selection by using the standard multiple-scale analysis [26–29], in which the control parameter(s) and the derivatives are expanded in terms of a small parameter ε and the Fredholm solubility condition is used. In the neighborhood of the bifurcation point (e.g., Hopf or Turing bifurcation point), the critical amplitudes A_j $(j = 1,2,3)$ follow the normal forms. Their general forms can be derived from the standard techniques of symmetry-breaking bifurcations. A normal form describes perfect extended patterns, but slight variations in the patterns can be included by means of spatial terms with suitable symmetries, so that one arrives at the amplitude equations [27,29,30].

However, the environments in models and laboratories are much less complex than ecological environments, and thus ecosystems can be modeled as open systems in which the interaction between the component parts is nonlinear and the interaction with the environment is noisy. Recently there has been a growth of interest in a deeper understanding of the role played by environmental noise in the dynamics of ecosystems [31–33]. The presence of noise in ecosystems gives rise to a rich variety of dynamical effects. The noise through its interaction with the nonlinearity of the living systems can cause new counterintuitive phenomena such as stochastic resonance [34–36], noise-enhanced stability [37,38], noise-delayed extinction [31,39,40], resonant activation [41,42], noise-induced transitions [43], and pattern formation [13,36,44–46].

*benguochong@163.com
†gquansun@yahoo.com.cn
‡Corresponding author: jinzhn@263.net

In this paper we mainly focus on the dynamics of pattern selection and noise-induced patterns in the Beddington-DeAngelis predator-prey system. The paper is organized as follows. In Sec. II we introduce the two-dimensional Beddington-DeAngelis predator-prey model and the zero-flux boundary conditions. In Sec. III we show the dynamical behaviors of the model in the absence of noise. We make a linear stability and obtain Turing bifurcation with zero-flux boundary conditions. Furthermore, we carry out a nonlinear analysis using multiple-scale analysis to derive the amplitude equations and also present and discuss the results of Turing pattern formation. In Sec. IV noise-induced patterns are exhibited through extensive numerical simulations. Finally, conclusions and discussions are presented in Sec. V.

II. THE MODEL

With the Beddington-DeAngelis or density-dependent functional response and logistic prey growth, we can establish a predator-prey model in the following form [47–53]:

$$\begin{aligned}\frac{dU}{dt} &= rU\left(1-\frac{U}{K}\right)-\frac{aUV}{b+U+cV},\\ \frac{dV}{dt} &= \frac{eaUV}{b+U+cV}-dV,\end{aligned} \tag{1}$$

where $U(t)$ and $V(t)$ stand for the prey and predator densities, respectively, at time t. The parameter r is the intrinsic growth rate of the prey, K is the carrying capacity of the prey, e is the conversion rate of prey to predator, and d is the mortality rate of the predator. The term $\frac{aU}{b+U+cV}$ is called the Beddington-DeAngelis functional response. The parameter a is the maximum number of prey that can be eaten by a predator per unit time, and the parameter b is the saturation constant. The parameter c scales the impact of the predator interference, and the term cV measures the mutual interference between predators.

In order to minimize the number of parameters involved in model (1), it is extremely useful to write the system in nondimensionalized form. We take

$$u=\frac{U}{K},\quad v=\frac{cV}{K},\quad d\sigma=\frac{adt}{c},$$

and then we have

$$\begin{aligned}\frac{du}{d\sigma} &= \alpha u(1-u)-\frac{uv}{\beta+u+v},\\ \frac{dv}{d\sigma} &= \frac{\gamma uv}{\beta+u+v}-\delta v,\end{aligned} \tag{2}$$

where $\alpha=\frac{cr}{a}$, $\beta=\frac{b}{K}$, $\gamma=ce$, and $\delta=\frac{cd}{a}$.

As shown in Refs. [54–56], by a change of the independent variable $d\sigma\to(\beta+u+v)d\sigma$ and still using the variable t instead of σ, model (2) is equivalent to the polynomial system

$$\begin{aligned}\frac{du}{dt} &= \alpha u(1-u)(\beta+u+v)-uv:=f(u,v),\\ \frac{dv}{dt} &= \gamma uv-\delta v(\beta+u+v):=g(u,v).\end{aligned} \tag{3}$$

When combined with the spatial factor, we have the following system:

$$\begin{aligned}\frac{\partial u}{dt} &= \alpha u(1-u)(\beta+u+v)-uv+d_1\nabla^2u,\\ \frac{\partial v}{dt} &= \gamma uv-\delta v(\beta+u+v)+d_2\nabla^2v,\end{aligned} \tag{4}$$

where the nonnegative constants d_1 and d_2 are, respectively, prey and predator diffusion coefficients. $\nabla^2=\frac{\partial^2}{\partial X^2+\partial Y^2}$ is the Laplacian operator in two-dimensional space.

To research the spatial effects due to the presence of noise, we consider a discrete-time evolution model (a coupled map lattice) [46,57]. The model with multiplicative noise corresponding to model (4) is given by

$$\begin{aligned}u_{i,j}^{n+1} &= \alpha u_{i,j}^n\left(1-u_{i,j}^n\right)\left(\beta+u_{i,j}^n+v_{i,j}^n\right)-u_{i,j}^nv_{i,j}^n\\ &\quad+u_{i,j}^nU_{i,j}^n+d_1\sum_p\left(u_p^n-u_{i,j}^n\right),\\ v_{i,j}^{n+1} &= \gamma u_{i,j}^nv_{i,j}^n-\delta v_{i,j}^n\left(\beta+u_{i,j}^n+v_{i,j}^n\right)\\ &\quad+v_{i,j}^nV_{i,j}^n+d_2\sum_p\left(v_p^n-v_{i,j}^n\right),\end{aligned} \tag{5}$$

where $u_{i,j}^n$ and $v_{i,j}^n$ represent, respectively, the densities of the prey and predator in the site (i,j) at the time step n. $\sum_p$ indicates the sum over the four nearest neighbors in the map lattice. White noise is the limiting case of colored noise, so we consider the more general case-colored noise in the present paper. The noise terms $U_{i,j}^n$ and $V_{i,j}^n$ are Ornstein-Uhlenbeck processes obeying the following statistical properties [46,58]:

$$\langle U(t)\rangle=\langle V(t)\rangle=0, \tag{6}$$

$$\langle U(t)U(t+\tau)\rangle=\langle V(t)V(t+\tau)\rangle=\frac{q}{2\tau_c}e^{-\tau/\tau_c}, \tag{7}$$

$$\left\langle U_{i,j}^nV_{i,j}^m\right\rangle=0,\quad\forall\, n,\,m,\,i,\,j, \tag{8}$$

where τ_c is the correlation time of the process and q is the noise intensity.

In the following sections, models (4) and (5) are to be analyzed under the following positive initial conditions and Neumann boundary conditions:

$$\begin{aligned}&u(X,Y,0)>0,\quad v(X,Y,0)>0,\\ &(X,Y)\in\Omega=[0,LX]\times[0,LY],\\ &\frac{\partial u}{\partial\mathbf{n}}=\frac{\partial v}{\partial\mathbf{n}}=0,(X,Y)\in\partial\Omega.\end{aligned} \tag{9}$$

In the above, LX and LY give the size of the system in the directions of X and Y, respectively, $\mathbf{n}$ is the outward unit normal vector of the boundary $\partial\Omega$, and we assume $\partial\Omega$ is smooth. The main reason for choosing such boundary conditions is that we are interested in the self-organization of the pattern. Neumann boundary conditions imply that the boundary of the model domain is simply reflective, and that the domain is isolated or insulated from the external environment [59]. At the same time, Neumann boundary conditions imply that there are no fluxes of populations through

the boundary; i.e., no external input is imposed from outside [9].

III. DYNAMICAL BEHAVIOR OF MODEL (4)

A. Linear stability analysis

In the absence of diffusion, model (4) corresponds to model (1). Recall that (u,v) is an equilibrium point of model (3) if it satisfies $f(u,v)=0$ and $g(u,v)=0$. Model (3) has two equilibrium solutions in the positive quadrant. One equilibrium point, given by $(u,v)=(1,0)$, is of no interest since it corresponds to the prey at its carrying capacity with no predator. Another equilibrium point is given by $E^*=(u^*,v^*)$, where

$$u^*=\frac{\alpha\gamma-\gamma+\delta+\sqrt{(\alpha\gamma-\gamma+\delta)^2+4\alpha\gamma\delta\beta}}{2\alpha\gamma},$$
$$v^*=\left(\frac{\gamma}{\delta}-1\right)u^*-\beta.$$

We can prove that it is necessary for β to be in the interval $(0,\frac{\gamma-\delta}{\delta})$ to ensure (u^*,v^*) a positive equilibrium. Moreover, (u^*,v^*) satisfies $|\mathbf{J}(u^*,v^*)|>0$, where $\mathbf{J}$ is the Jacobian matrix of model (3). The proof can be seen in Appendix A.

From the biological perspective, we are interested in studying the stability behavior of the interior equilibrium point E^*. The Jacobian matrix corresponding to this equilibrium point is as follows:

$$\mathbf{J}=\begin{pmatrix}a_{11}&a_{12}\\a_{21}&a_{22}\end{pmatrix},$$

where

$$\begin{aligned}a_{11}&=\alpha(1-u^*)(\beta+u^*+v^*)-\alpha u^*(\beta+u^*+v^*)\\&\quad+\alpha u^*(1-u^*)-v^*,\\a_{12}&=\alpha u^*(1-u^*)-u^*,\\a_{21}&=\gamma v^*-\delta v^*,\\a_{22}&=\gamma u^*-\delta(\beta+u^*+v^*)-\delta v^*.\end{aligned}\tag{10}$$

The Turing condition is the one in which the uniform steady state of the RD system is stable for the corresponding ordinary differential equations, but it is unstable in the partial differential equations with diffusion terms. First, we address the temporal stability of the uniform state to nonuniform perturbations [60]:

$$\begin{pmatrix}u\\v\end{pmatrix}=\begin{pmatrix}u^*\\v^*\end{pmatrix}+\varepsilon\begin{pmatrix}u_k\\v_k\end{pmatrix}e^{\lambda t+i\boldsymbol{k}\cdot\boldsymbol{r}}+\text{c.c.}+O(\varepsilon^2),\tag{11}$$

where λ is the growth rate of perturbations in time t, i is the imaginary unit and $i^2=-1$, $\boldsymbol{k}\cdot\boldsymbol{k}=k^2$ and k is the wave number, $\boldsymbol{r}=(X,Y)$ is the spatial vector in two dimensions, and c.c. stands for the complex conjugate. The linear instability ($\varepsilon\ll 1$) of the uniform state is deduced from the dispersion relations. After substituting Eq. (7) into Eq. (4), one finds the characteristic equation for the growth rate λ as the determinant $\det\mathbf{A}$, where

$$\mathbf{A}=\begin{pmatrix}a_{11}-d_1k^2-\lambda&a_{12}\\a_{21}&a_{22}-d_2k^2-\lambda\end{pmatrix}.$$

Then we can obtain the eigenvalues λ_k as follows:

$$\lambda_k=\frac{tr_k\pm\sqrt{(tr_k)^2-4\Delta_k}}{2},\tag{12}$$

where

$$\begin{aligned}tr_k&=a_{11}+a_{22}-k^2(d_1+d_2)=tr_{\mathbf{J}}-k^2(d_1+d_2),\\\Delta_k&=a_{11}a_{22}-a_{12}a_{21}-k^2(a_{11}d_2+a_{22}d_1)+k^4d_1d_2\\&=\Delta_{\mathbf{J}}-k^2(a_{11}d_2+a_{22}d_1)+k^4d_1d_2.\end{aligned}$$

Hopf bifurcation occurs when $\mathrm{Im}(\lambda_k)\neq 0$, $\mathrm{Re}(\lambda_k)=0$, at $k=0$; i.e., $a_{11}+a_{22}=0$. Then we can get the critical value of the Hopf bifurcation parameter β_H:

$$\beta_H=\frac{\gamma^2-\alpha\gamma^2-\gamma^2\delta+\alpha\gamma^3-\gamma^3+\delta\gamma^3-\delta^2+2\gamma\delta^2-\delta^2\gamma^2}{(-\gamma-\delta+\delta\gamma)^2}.\tag{13}$$

Turing bifurcation occurs when $\mathrm{Im}(\lambda_k)=0$, $\mathrm{Re}(\lambda_k)=0$, at $k=k_T\neq 0$, and the wave number k_T satisfies

$$k_T^2=\sqrt{\frac{\Delta_{\mathbf{J}}}{d_1d_2}}=\sqrt{\frac{u^*v^*\sqrt{(\alpha\gamma-\gamma+\delta)^2+4\alpha\gamma\delta\beta}}{d_1d_2}}.\tag{14}$$

We can obtain the critical value of the Turing bifurcation parameter β_T. Since β_T is too long, we do not show its accurate expression in this paper. At the Turing bifurcation threshold, the spatial symmetry of the system is broken, and the patterns are stationary in time and oscillatory in space with the corresponding wavelength $\lambda_T=\frac{2\pi}{k_T}$ [61–63].

Now, let us discuss the bifurcations represented by these formulas in the parameter region spanned by the parameters α and β that can be seen from Fig. 1. All of the spatial models are induced in this parameter region. For overall analysis, we show the real part of the eigenvalue as β is decreased, which can be seen in Fig. 2

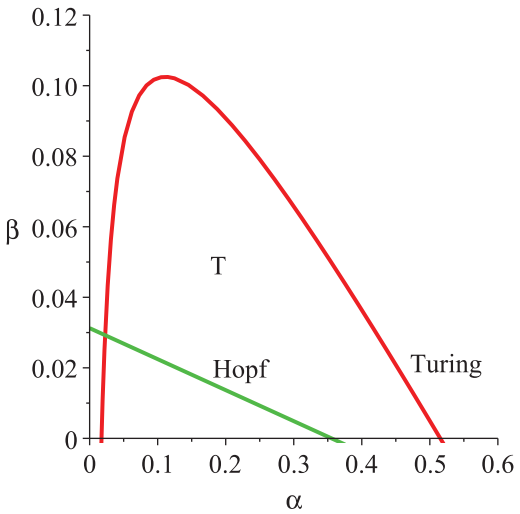

FIG. 1. (Color online) Bifurcation diagram of model (4). We set the parameter values as $\delta=0.6,\gamma=0.9,d_1=0.01,d_2=1$. The figure shows the Turing space (marked T), i.e., the region bounded by the Turing bifurcation line (the red (upper) line) and the Hopf bifurcation line (the green (light gray) line).

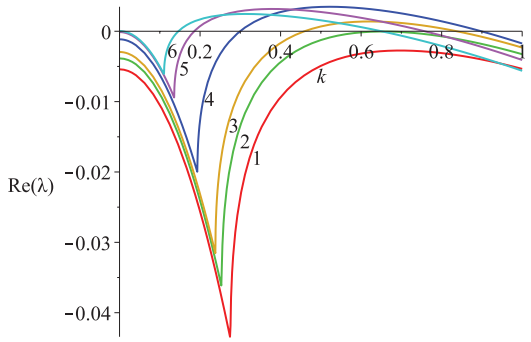

FIG. 2. (Color online) The real part of the eigenvalue as β is decreased. We set the parameter values as $\alpha = 0.095, \delta = 0.6, \gamma = 0.9, d_1 = 0.01, d_2 = 1$. The value of β is as follows: 1: $\beta = 0.12$; 2: $\beta = 0.102$; 3: $\beta = 0.09$; 4: $\beta = 0.06$; 5: $\beta = 0.03$; 6: $\beta = 0.02$.

B. Spatial dynamics of model (4)

1. Amplitude equations

The standard multiple-scale analysis yields the well-known amplitude equations [27,29,30]. This method is based on the fact that near the instability threshold the basic state is unstable only in regard to perturbations with wave numbers close to the critical value k_T [defined as Eq. (14)]. In other words, close to the onset $\beta = \beta_T$, the eigenvalues associated with the critical modes are close to zero, and they are slowly varying modes, whereas the off-critical modes relax quickly, so only perturbations with k around k_T need considering. The whole dynamics can be therefore reduced to the dynamics of the active slow modes [64]. The stability and selection of different patterns close to the onset can be derived from the amplitude equations that govern the dynamics of these active modes. Turing patterns (e.g., hexagon and stripe patterns) are thus well described by a system of three active resonant pairs of modes $(\boldsymbol{k}_j, -\boldsymbol{k}_j)$ $(j = 1,2,3)$ making angles of $2\pi/3$ and $|\boldsymbol{k}_j| = k_T$.

In order to obtain the amplitude equations, we should first write the linearized form of model (4) at the equilibrium point E^* as follows:

$$\begin{aligned}\frac{\partial x}{dt} &= a_{11}x + a_{12}y + \alpha\left[1 - \left(\frac{\gamma}{\delta} + 2\right)u^*\right]x^2 \\ &\quad + [\alpha(1-2u^*) - 1]xy - \alpha x^2 y - \alpha x^3 + d_1\nabla^2 x, \\ \frac{\partial y}{dt} &= a_{21}x + a_{22}y + (\gamma - \delta)xy - \delta y^2 + d_2\nabla^2 y. \end{aligned} \quad (15)$$

Close to onset $\beta = \beta_T$, the solutions of model (4) can be expanded as

$$\boldsymbol{U} = \boldsymbol{U}_S + \sum_{j=1}^{3} \boldsymbol{U}_0[A_j \exp(i\boldsymbol{k}_j \cdot \boldsymbol{r}) + \bar{A}_j \exp(-i\boldsymbol{k}_j \cdot \boldsymbol{r})]. \quad (16)$$

At the same time, the solutions of model (15) can be expanded as

$$\boldsymbol{U}^0 = \sum_{j=1}^{3} \boldsymbol{U}_0[A_j \exp(i\boldsymbol{k}_j \cdot \boldsymbol{r}) + \bar{A}_j \exp(-i\boldsymbol{k}_j \cdot \boldsymbol{r})], \quad (17)$$

where $\boldsymbol{U}_S$ represents the uniform steady state and $\boldsymbol{U}_0 = [(a_{11}^* d_2 + a_{22}^* d_1)/(2a_{21}^* d_1), 1]^T$ is the eigenvector of the linearized operator. In other words, $\boldsymbol{U}_0$ defines the direction of the eigenmodes in concentration space (i.e., the ratio of x and y). A_j and the conjugate $\bar{A}_j$ are, respectively, the amplitudes associated with the modes $\boldsymbol{k}_j$ and $-\boldsymbol{k}_j$. From the standard multiple-scale analysis, up to the third order in the perturbations, the spatiotemporal evolution of the amplitudes A_j is described through the equations, i.e., amplitude equations:

$$\begin{aligned}\tau_0\frac{\partial A_1}{dt} &= \mu A_1 + h\bar{A}_2\bar{A}_3 - [g_1|A_1|^2 + g_2(|A_2|^2 + |A_3|^2)]A_1, \\ \tau_0\frac{\partial A_2}{dt} &= \mu A_2 + h\bar{A}_1\bar{A}_3 - [g_1|A_2|^2 + g_2(|A_1|^2 + |A_3|^2)]A_2, \\ \tau_0\frac{\partial A_3}{dt} &= \mu A_3 + h\bar{A}_1\bar{A}_2 - [g_1|A_3|^2 + g_2(|A_1|^2 + |A_2|^2)]A_3, \end{aligned} \quad (18)$$

where $\mu = (\beta_T - \beta)/\beta_T$ is a normalized distance to onset and τ_0 is a typical relaxation time. Notably, for model (15), the distance to onset, μ, increases when the bifurcation parameter β decreases.

The form of Eqs. (18) is general for Turing bifurcation, but the exact expressions of the coefficients are specific to the model. Next, we will obtain the exact but complex expressions of the coefficients τ_0, h, g_1, and g_2. The parameters that do not appear in the above will be explained in Appendix B.

Setting $\boldsymbol{X} = (x,y)^T$, $\boldsymbol{N} = (N_1, N_2)$, model (15) can be converted to the following system:

$$\frac{\partial \boldsymbol{X}}{\partial t} = \boldsymbol{L}\boldsymbol{X} + \boldsymbol{N}, \quad (19)$$

where

$$\boldsymbol{L} = \begin{pmatrix} a_{11} + d_1\nabla^2 & a_{12} \\ a_{21} & a_{22} + d_2\nabla^2 \end{pmatrix},$$

$$\boldsymbol{N} = \begin{pmatrix} N_1 \\ N_2 \end{pmatrix} = \begin{pmatrix} \alpha\left[1 - \left(\frac{\gamma}{\delta} + 2\right)u^*\right]x^2 + [\alpha(1-2u^*) - 1]xy - \alpha x^2 y - \alpha x^3 \\ (\gamma - \delta)xy - \delta y^2 \end{pmatrix}.$$

During the calculation, we just analysis the behavior of the controlled parameter close to onset $\beta = \beta_T$. With this method, we can expand β in the following term:

$$\beta_T - \beta = \varepsilon\beta_1 + \varepsilon^2\beta_2 + \varepsilon^3\beta_3 + O(\varepsilon^4), \quad (20)$$

where ε is a small parameter. Expanding the variable $\boldsymbol{X}$ and the nonlinear term $\boldsymbol{N}$ according to this small parameter, we have the following results:

$$\boldsymbol{X} = \begin{pmatrix} x \\ y \end{pmatrix} = \varepsilon \begin{pmatrix} x_1 \\ y_1 \end{pmatrix} + \varepsilon^2 \begin{pmatrix} x_2 \\ y_2 \end{pmatrix} + \varepsilon^3 \begin{pmatrix} x_3 \\ y_3 \end{pmatrix} + O(\varepsilon^4), \quad (21)$$

$$\boldsymbol{N} = \varepsilon^2 \boldsymbol{h}^2 + \varepsilon^3 \boldsymbol{h}^3 + O(\varepsilon^4), \quad (22)$$

where $\boldsymbol{h}^2$ and $\mathbf{h}^3$ are corresponding to the second and the third orders of ε in the expansion of the nonlinear term $\boldsymbol{N}$. At the same time, the linear operator $\boldsymbol{L}$ can be expanded as follows:

$$\boldsymbol{L} = \boldsymbol{L}_T + (\beta_T - \beta)\boldsymbol{M}, \quad (23)$$

where

$$\boldsymbol{L}_T = \begin{pmatrix} a_{11}^* + d_1\nabla^2 & a_{12}^* \\ a_{21}^* & a_{22}^* + d_2\nabla^2 \end{pmatrix}, \quad \boldsymbol{M} = \begin{pmatrix} b_{11} & b_{12} \\ b_{21} & b_{22} \end{pmatrix}.$$

The core of the standard multiple-scale analysis is separating the dynamical behavior of the system according to different time scale or spatial scale. We just need to separate the time scale for model (19) (i.e., $T_0 = t$, $T_1 = \varepsilon t$, $T_2 = \varepsilon^2 t$). Each time scale T_i can be considered as an independent variable. T_i corresponds to the dynamical behaviors of the variables whose scales are ε^{-i}. So the derivative with respect to time converts to the following term:

$$\frac{\partial}{\partial t} = \frac{\partial}{\partial T_0} + \varepsilon \frac{\partial}{\partial T_1} + \varepsilon^2 \frac{\partial}{\partial T_2} + O(\varepsilon^3). \quad (24)$$

For solution (17), we can consider the foundation of the solution independent of time. As amplitude A is a variable that changes slowly, the derivative with respect to time $\frac{\partial}{\partial T_0}$ that corresponds to the variable that changes fast does not have an effect on the amplitude A. Then we have the following result:

$$\frac{\partial A}{\partial t} = \varepsilon \frac{\partial A}{\partial T_1} + \varepsilon^2 \frac{\partial A}{\partial T_2} + O(\varepsilon^3). \quad (25)$$

Substituting Eqs. (21), (22), (23), and (24) into Eq. (19) and expanding Eq. (19) according to different orders of ε, we can obtain three equations as follows:
The first order of ε:

$$\boldsymbol{L}_T \begin{pmatrix} x_1 \\ y_1 \end{pmatrix} = 0;$$

The second order of ε:

$$\boldsymbol{L}_T \begin{pmatrix} x_2 \\ y_2 \end{pmatrix} = \frac{\partial}{\partial T_1} \begin{pmatrix} x_1 \\ y_1 \end{pmatrix} - \beta_1 \boldsymbol{M} \begin{pmatrix} x_1 \\ y_1 \end{pmatrix} - \boldsymbol{h}_2;$$

The third order of ε:

$$\boldsymbol{L}_T \begin{pmatrix} x_3 \\ y_3 \end{pmatrix} = \frac{\partial}{\partial T_1} \begin{pmatrix} x_2 \\ y_2 \end{pmatrix} + \frac{\partial}{\partial T_2} \begin{pmatrix} x_1 \\ y_1 \end{pmatrix} - \beta_1 \boldsymbol{M} \begin{pmatrix} x_2 \\ y_2 \end{pmatrix} - \beta_2 \boldsymbol{M} \begin{pmatrix} x_1 \\ y_1 \end{pmatrix} - \boldsymbol{h}_3.$$

For the first order of ε:

$$\boldsymbol{L}_T \begin{pmatrix} x_1 \\ y_1 \end{pmatrix} = 0. \quad (26)$$

As $\boldsymbol{L}_T$ is the linear operator of the system close to the onset, $(x_1, y_1)^T$ is the linear combination of the eigenvectors that corresponds to the eigenvalue 0. Solving the first order of ε, we have

$$\begin{pmatrix} x_1 \\ y_1 \end{pmatrix} = \begin{pmatrix} \frac{a_{11}^* d_2 - a_{22}^* d_1}{2a_{21}^* d_1} \\ 1 \end{pmatrix} [W_1 \exp(i\boldsymbol{k}_1 \boldsymbol{r}) + W_2 \exp(i\boldsymbol{k}_2 \boldsymbol{r}) + W_3 \exp(i\boldsymbol{k}_3 \boldsymbol{r})] + \text{c.c.}, \quad (27)$$

where $|\boldsymbol{k}_j| = k_T^*$, W_j is the amplitude of the mode $\exp(i\boldsymbol{k}_j \boldsymbol{r})$ when the system is under the first-order perturbation. Its form is determined by the perturbational term of the higher order.

For the second order of ε, we have

$$\boldsymbol{L}_T \begin{pmatrix} x_2 \\ y_2 \end{pmatrix} = \frac{\partial}{\partial T_1} \begin{pmatrix} x_1 \\ y_1 \end{pmatrix} - \beta_1 \begin{pmatrix} b_{11}x_1 + b_{12}y_1 \\ b_{21}x_1 + b_{22}y_1 \end{pmatrix} - \begin{pmatrix} \{\alpha[1 - (\frac{\gamma}{\delta} + 2)\frac{\alpha\gamma - \gamma + \delta + c}{2\alpha\gamma}]x_1^2 + (\alpha - 1 - \frac{\alpha\gamma - \gamma + \delta + c}{\gamma})x_1 y_1 \\ (\gamma - \delta)x_1 y_1 - \delta y_1^2 \end{pmatrix} = \begin{pmatrix} F_x \\ F_y \end{pmatrix}. \quad (28)$$

According to the Fredholm solubility condition, the vector function of the right-hand side of Eq. (28) must be orthogonal with the zero eigenvectors of operator $\boldsymbol{L}_c^+$ to ensure the existence of the nontrivial solution of this equation. $\boldsymbol{L}_c^+$ is the adjoint operator of $\boldsymbol{L}_c$. In this system the zero eigenvectors of operator $\boldsymbol{L}_c^+$ are

$$\begin{pmatrix} 1 \\ -\frac{2a_{21}^* d_2}{a_{11}^* d_2 - a_{22}^* d_1} \end{pmatrix} \exp(-i\boldsymbol{k}_j \boldsymbol{r}) + \text{c.c.}, \quad j = 1,2,3. \quad (29)$$

The orthogonality condition is

$$\left(1, -\frac{2a_{21}^* d_2}{a_{11}^* d_2 - a_{22}^* d_1}\right) \begin{pmatrix} F_x^i \\ F_y^i \end{pmatrix} = 0, \quad (30)$$

where F_x^i and F_y^i, separately, represent the coefficients corresponding to $\exp(i\boldsymbol{k}_j \boldsymbol{r})$ in F_x and F_y. Taking $\exp(i\boldsymbol{k}_1 \boldsymbol{r})$, for example, we have

$$\begin{pmatrix} F_x^1 \\ F_x^2 \end{pmatrix} = \begin{pmatrix} l\frac{\partial W_1}{\partial T_1} \\ \frac{\partial W_1}{\partial T_1} \end{pmatrix} - \beta_1 \begin{pmatrix} b_{11}lw_1 + b_{12}w_1 \\ b_{21}lw_1 + b_{22}w_1 \end{pmatrix} - \begin{pmatrix} 2\alpha l^2[1 - (\frac{\gamma}{\delta} + 2)\frac{\alpha\gamma - \gamma + \delta + c}{2\alpha\gamma}]\bar{W}_2\bar{W}_3 + 2l(\alpha - 1 - \frac{\alpha\gamma - \gamma + \delta + c}{\gamma})\bar{W}_2\bar{W}_3 \\ 2l(\gamma - \delta)\bar{W}_2\bar{W}_3 - 2\delta\bar{W}_2\bar{W}_3 \end{pmatrix}. \quad (31)$$

Using the orthogonality condition, we can obtain the following result:

$$\frac{d_2-d_1}{d_2}l\frac{\partial W_1}{\partial T_1}=\beta_1\left[lb_{11}+b_{12}-\frac{d_1}{d_2}l(lb_{21}+b_{22})\right]W_1+\left\{2\alpha dl^2+2el-\frac{d_1}{d_2}l[2l(\gamma-\delta)-2\delta]\right\}\bar{W}_2\bar{W}_3. \tag{32}$$

The other two equations can be obtained through the transformation of the subscript of W. Solving Eq. (28), we have

$$\begin{aligned}\begin{pmatrix}x_2\\y_2\end{pmatrix}&=\begin{pmatrix}X_0\\Y_0\end{pmatrix}+\sum_{j=1}^{3}\begin{pmatrix}X_j\\Y_j\end{pmatrix}\exp(i\boldsymbol{k}_j\boldsymbol{r})+\sum_{j=1}^{3}\begin{pmatrix}X_{jj}\\Y_{jj}\end{pmatrix}\exp(i2\boldsymbol{k}_j\boldsymbol{r})\\&+\begin{pmatrix}X_{12}\\Y_{12}\end{pmatrix}\exp[i(\boldsymbol{k}_1-\boldsymbol{k}_2)\boldsymbol{r}]+\begin{pmatrix}X_{23}\\Y_{23}\end{pmatrix}\exp[i(\boldsymbol{k}_2-\boldsymbol{k}_3)\boldsymbol{r}]+\begin{pmatrix}X_{31}\\Y_{31}\end{pmatrix}\exp[i(\boldsymbol{k}_3-\boldsymbol{k}_1)\boldsymbol{r}]+\text{c.c.}\end{aligned} \tag{33}$$

The coefficients in Eq. (33) are obtained by solving the sets of the linear equations about $\exp(0)$, $\exp(i\boldsymbol{k}_j\boldsymbol{r})$, $\exp(i2\boldsymbol{k}_j\boldsymbol{r})$, and $\exp(i(\boldsymbol{k}_j-\boldsymbol{k}_k)\boldsymbol{r})$. With this method, we have

$$\begin{pmatrix}X_0\\Y_0\end{pmatrix}=\begin{pmatrix}x_0\\y_0\end{pmatrix}(|W_1|^2+|W_2|^2+|W_3|^2),X_i=lY_i,$$
$$\begin{pmatrix}X_{jj}\\Y_{jj}\end{pmatrix}=\begin{pmatrix}x_{11}\\y_{11}\end{pmatrix}W_j^2,\begin{pmatrix}X_{jk}\\Y_{jk}\end{pmatrix}=\begin{pmatrix}x^*\\y^*\end{pmatrix}W_j\bar{W}_k.$$

For the third order of ε, we have

$$\begin{aligned}\boldsymbol{L}_T\begin{pmatrix}x_3\\y_3\end{pmatrix}&=\frac{\partial}{\partial T_1}\begin{pmatrix}x_2\\y_2\end{pmatrix}-\beta_1\begin{pmatrix}b_{11}x_2+b_{12}y_2\\b_{21}x_2+b_{22}y_2\end{pmatrix}-\beta_2\begin{pmatrix}b_{11}x_1+b_{12}y_1\\b_{21}x_1+b_{22}y_1\end{pmatrix}\\&-\begin{pmatrix}2\alpha\left[1-\left(\frac{\gamma}{\delta}+2\right)\frac{\alpha\gamma-\gamma+\delta+c}{2\alpha\gamma}\right]x_1x_2+\left(\alpha-1-\frac{\alpha\gamma-\gamma+\delta+c}{\gamma}\right)(x_1y_2+x_2y_1)\\(\gamma-\delta)(x_1y_2+x_2y_1)-2\delta y_1y_2\end{pmatrix}-\begin{pmatrix}\alpha x_1^2y_1+\alpha x_1^3\\0\end{pmatrix}.\end{aligned} \tag{34}$$

Using the Fredholm solubility condition again, we can obtain

$$\begin{aligned}&\frac{d_2-d_1}{d_2}l\frac{\partial W_1}{\partial T_2}+\frac{d_2-d_1}{d_2}l\frac{\partial Y_1}{\partial T_1}\\&=\beta_2\left[lb_{11}+b_{12}-\frac{d_1}{d_2}l(lb_{21}+b_{22})\right]W_1+\beta_1\left[lb_{11}+b_{12}-\frac{d_1}{d_2}l(lb_{21}+b_{22})\right]Y_1\\&+\left\{2\alpha dl^2+2el-\frac{d_1}{d_2}l[2l(\gamma-\delta)-2\delta]\right\}(\bar{W}_2\bar{Y}_3+\bar{W}_3\bar{Y}_2)-[G_1|W_1|^2+G_2(|W_2|^2+|W_3|^2)]W_1.\end{aligned} \tag{35}$$

The other two equations can be obtained through the transformation of the subscript of W. The amplitude A_i can be expanded as

$$A_i=\varepsilon W_i+\varepsilon^2V_i+O(\varepsilon^3). \tag{36}$$

Equations (32) and (35) separately multiplying by ε^2 and ε^3, and using Eqs. (25) and (36) to merge the variables, we can obtain the amplitude equation corresponding to A_1 as follows:

$$\begin{aligned}\tau_0\frac{\partial A_1}{\partial t}&=\mu A_1+h\bar{A}_2\bar{A}_3\\&-[g_1|A_1|^2+g_2(|A_2|^2+|A_3|^2)]A_1.\end{aligned} \tag{37}$$

The other two equations of Eqs. (18) can be obtained through the transformation of the subscript of A. The exact expressions of the coefficients τ_0,h,g_1, and g_2 are shown in Appendix B.

2. *Amplitude instability*

Each amplitude in Eqs. (18) can be decomposed to mode $\rho_i=|A_i|$ and a corresponding phase angle φ_i. Then, substituting $A_i=\rho_i\exp(i\varphi_i)$ into Eqs. (18) and separating the real and imaginary parts, we can get four differential equations of the real variables as follows:

$$\begin{aligned}\tau_0\frac{\partial\varphi}{dt}&=-h\frac{\rho_1^2\rho_2^2+\rho_1^2\rho_3^2+\rho_2^2\rho_3^2}{\rho_1\rho_2\rho_3}\sin\varphi,\\\tau_0\frac{\partial\rho_1}{dt}&=\mu\rho_1+h\rho_2\rho_3\cos\varphi-g_1\rho_1^3-g_2(\rho_2^2\rho_3^2)\rho_1,\\\tau_0\frac{\partial\rho_2}{dt}&=\mu\rho_2+h\rho_1\rho_3\cos\varphi-g_1\rho_2^3-g_2(\rho_1^2\rho_3^2)\rho_2,\\\tau_0\frac{\partial\rho_3}{dt}&=\mu\rho_3+h\rho_1\rho_2\cos\varphi-g_1\rho_3^3-g_2(\rho_1^2\rho_2^2)\rho_3,\end{aligned} \tag{38}$$

where $\varphi=\varphi_1+\varphi_2+\varphi_3$.

The dynamical system (38) possesses five kinds of solutions [65].

(1) The stationary state (O), given by

$$\rho_1=\rho_2=\rho_3=0, \tag{39}$$

is stable for $\mu<\mu_2=0$ and unstable for $\mu>\mu_2$.

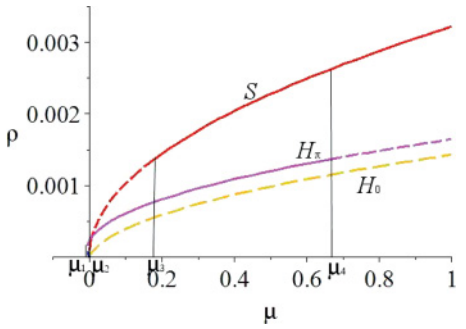

FIG. 3. (Color online) Bifurcation diagram of model (4). We set the parameter values as $\alpha = 0.095, \delta = 0.6, \gamma = 0.9, d_1 = 0.01, d_2 = 1$. H_0: hexagon patterns with $\varphi = 0$; H_π: hexagon patterns with $\varphi = \pi$; S: stripe patterns. Solid curve: stable state; dashed line: unstable state. $\mu_1 = -0.005027870678$, $\mu_2 = 0$, $\mu_3 = 0.1786762799$, $\mu_4 = 0.6618985686$.

(2) Stripe patterns(S), given by

$$\rho_1 = \sqrt{\frac{\mu}{g_1}} \neq 0, \quad \rho_2 = \rho_3 = 0, \tag{40}$$

are stable for $\mu > \mu_3 = \frac{h^2 g_1}{(g_2 - g_1)^2}$ and unstable for $\mu < \mu_3$.

(3) Hexagon patterns (H_0, H_π) are given by

$$\rho_1 = \rho_2 = \rho_3 = \frac{|h| \pm \sqrt{h^2 + 4(g_1 + 2g_2\mu)}}{2(g_1 + 2g_2)}, \tag{41}$$

with $\varphi = 0$ or π, and exist when

$$\mu > \mu_1 = \frac{-h^2}{4(g_1 + 2g_2)}. \tag{42}$$

The solution $\rho^+ = \frac{|h| + \sqrt{h^2 + 4(g_1 + 2g_2\mu)}}{2(g_1 + 2g_2)}$ is stable only for

$$\mu < \mu_4 = \frac{2g_1 + g_2}{(g_2 - g_1)^2} h^2, \tag{43}$$

and $\rho^- = \frac{|h| - \sqrt{h^2 + 4(g_1 + 2g_2\mu)}}{2(g_1 + 2g_2)}$ is always unstable.

(4) The mixed states are given by

$$\rho_1 = \frac{|h|}{g_2 - g_1}, \quad \rho_2 = \rho_3 = \sqrt{\frac{\mu - g_1\rho_1^2}{g_1 + g_2}}, \tag{44}$$

with $g_2 > g_1$. They exist when $\mu > \mu_3$ and are always unstable.

The analysis results from the above can be seen in Fig. 3. When the control parameter μ increases to the critical point $\mu_2 = 0$, the stationary state of the system begins to lose stability. The system first form hexagon patterns through the nonequilibrium phase transition. If the coefficient h of the second term in Eq. (37) is greater than zero, the hexagon patterns are H_0 (i.e., $\varphi = 0$). On the other hand, the hexagon patterns are H_π (i.e., $\varphi = \pi$). In the former case, $\varphi = \pi$ is always unstable. In the latter case, $\varphi = 0$ is always unstable. The emergence of hexagon patterns is caused by subcritical bifurcation. In other words, the system exists a bistable region in the range of the control parameter (i.e., $\mu_1 < \mu < \mu_2$). The hexagon patterns and the stationary state are all stable in this region. The emergence of stripe patterns derives from supercritical bifurcation. But they are unstable for $\mu < \mu_3$, and they are stable only for $\mu > \mu_3$. Because the hexagon patterns lose stability only for $\mu > \mu_4$, the system exists in another bistable state (i.e., the bistable state between the hexagon patterns and the stripe patterns) when the control parameter lies in the range $\mu_3 < \mu < \mu_4$. The system transfers to the stripe patterns from the hexagon patterns when the control parameter μ exceeds μ_4. In another case, the system transfers to the hexagon patterns from the stripe patterns when μ decreases to the level less than μ_3.

3. *Pattern formation of model (4)*

In this section we perform extensive numerical simulations of the spatially extended model (4) in two-dimensional spaces, and the qualitative results are shown here. All our numerical simulations employ the Neumann boundary conditions with a system size of 200×200. The space step is $d\boldsymbol{r} = 1.25$, and the time step is $dt = 0.05$.

We keep $\alpha = 0.095$, $\delta = 0.6$, $\gamma = 0.9$, $d_1 = 0.01$, $d_2 = 1$. Then we can find that $g_1 = 97025.80711, g_2 = 165376.3004$, $h = -92.75375240$, $\mu_1 = -0.005027870678$, $\mu_2 = 0$, $\mu_3 = 0.1786762799$, and $\mu_4 = 0.6618985686$. Obviously the parameter values of g_1, g_2, and h have the following relations: $g_2 > g_1 > 0$ and $g_2 > g_1 \gg |h|$. Otherwise it is necessary to include some other terms up to the fourth order or higher. At the same time, we know that when $\mu = \mu_2, \mu_3$, and μ_4, the corresponding values of β are $\beta = 0.1017547291, 0.08357357133$, and 0.03440341948, respectively.

Initially the system is placed in the stationary state (u^*, v^*). We run the numerical simulations until they reach a stationary state or until they show a behavior that does not seem to change its characteristics any longer. In the numerical simulations, different types of dynamics are observed, and we have found that the distributions of u and v are always of the same type. Consequently we can restrict our analysis of pattern formation to one distribution. In this paper we just show the distribution of v. Next, we will show the Turing patterns for the parameters (α, β) located in the Turing space.

The parameter values of Figs. 4–6 are in the domain of Turing space. All of the figures show the evolution of the spatial patterns of the 0, 10 000, 100 000, 200 000, 300 000, and 400 000 iterations, with random small perturbation of the stationary solution (u^*, v^*) of the spatially homogeneous system.

From Fig. 4 we can see that the H_π hexagon patterns prevail over the whole domain finally, and the dynamics of the system does not undergo any further changes. The parameter values set in Fig. 4 satisfy $\mu_2 < \mu = 0.03689979760 < \mu_3$. As $h = -92.75375240 < 0$, we can obtain that it just emerges H_π hexagon patterns under this circumstance according to the analysis above. That is to say, the numerical simulation is compatible with the theoretical analysis. At the same time, we should pay attention to the situation that μ is very close to μ_2; i.e., β is very close to the Turing bifurcation line in the Turing space. Under this circumstance, the stationary state begins to lose stability and the H_π hexagon patterns come into being very slowly. This is the universal phenomenon of critical slowing down.

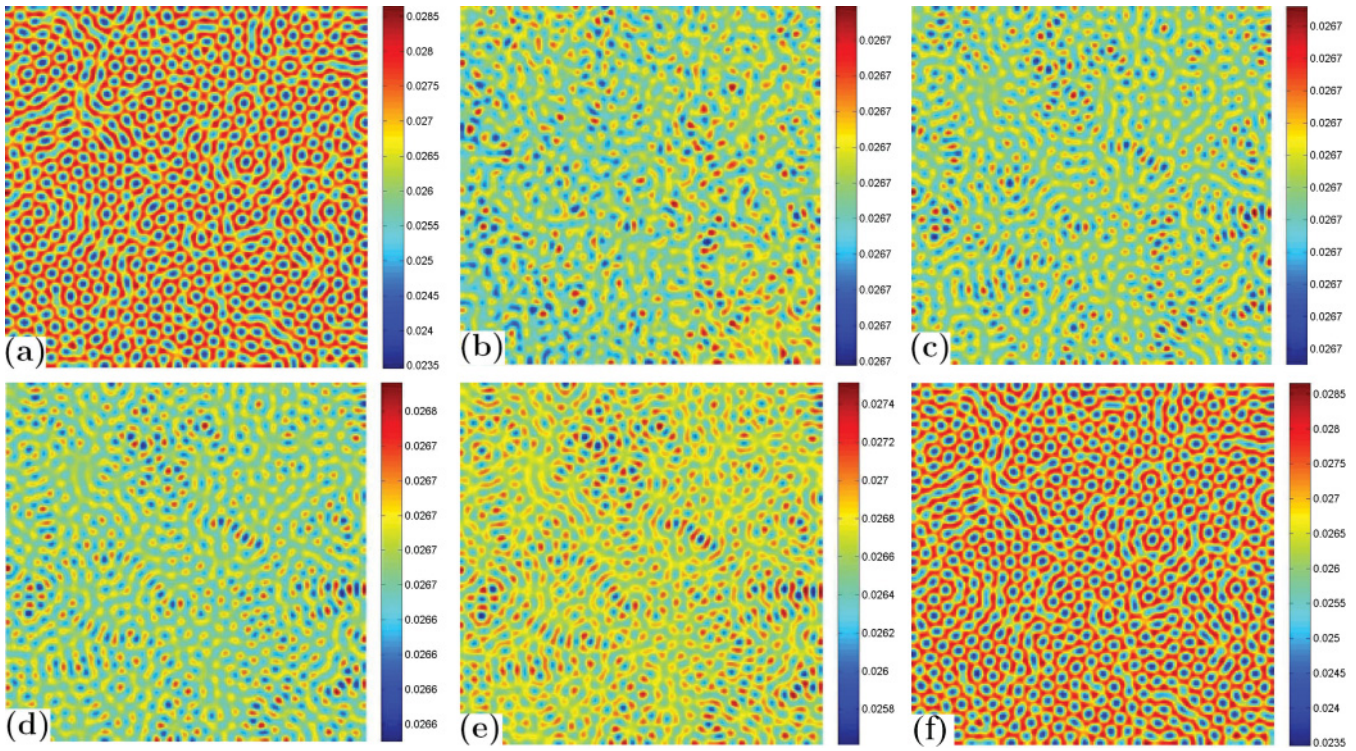

FIG. 4. (Color online) Snapshots of contour pictures of the time evolution of v at different instants with $\alpha = 0.095, \delta = 0.6, \gamma = 0.9, d_1 = 0.01, d_2 = 1, \beta = 0.098$ and the parameter values in the Turing space. (a) 0 iteration; (b) 10 000 iterations; (c) 100 000 iterations; (d) 200 000 iterations; (e) 300 000 iterations; (f) 400 000 iterations.

Figure 5 shows that stationary stripe patterns and H_0 hexagon patterns emerge mixed in the distribution of the predator quantity. The parameter values set in Fig. 5 satisfy $\mu_3 < \mu = 0.2629335186 < \mu_4$. The numerical simulation is corresponding to the theoretical analysis. The system is bistable, and these two kinds of patterns can exist at the same time. This phenomenon is called the pinning effect [66]. When μ increases to the second critical point μ_3, the hexagon patterns begin to lose stability, and the system transfer to the stripe patterns from the hexagon patterns gradually.

Figure 6 shows that there are only H_0 hexagon patterns in the distribution of the predator quantity. The parameter values set in Fig. 6 satisfy $\mu = 0.7543111731 > \mu_4$. The numerical simulation cannot correspond to the theoretical analysis. This phenomenon cannot be explained by the amplitude equations. This is the reentry of the hexagon patterns and can be explained as follows: When the system gets away from the Turing critical bifurcation line, some of the primary slave modes turn into active modes. We cannot adiabatically eliminate them when deducing the amplitude equations. On the contrary, we should add them into the amplitude equations. When the uniform-state mode with $\mathbf{0}(|\boldsymbol{k}| = 0)$ turns into the active mode, another third-order term, $A_0\bar{A}_2\bar{A}_3$, is added into the amplitude equation of A_1. This term satisfies the resonance relation $\boldsymbol{k}_1 = -\boldsymbol{k}_2 - \boldsymbol{k}_3 + \mathbf{0}$ (the angles of $\boldsymbol{k}_1, \boldsymbol{k}_2$ and $\boldsymbol{k}_3$ are all $2\pi/3$). At the same time, $A_0\bar{A}_1\bar{A}_3$ and $A_0\bar{A}_1\bar{A}_2$ are added into the amplitude equations of A_2 and A_3. These new terms result in the stability of the hexagon patterns again [65].

To gain more insight into the patterns, we perform the power spectra of the simulation patterns using the two-dimensional Fourier transform. In Fig. 7 we show our three simulation patterns with their two-dimensional power spectra for $\beta = 0.098, 0.075$, and 0.025, respectively. For $\beta = 0.098$ and 0.075, the figures have similar spatial frequency in the length of the space unit, and they present one mode with different wave numbers. For $\beta = 0.025$, we find that the figure has two modes with different wave numbers.

IV. PATTERN FORMATION OF MODEL (5)

In this section we rely on numerical integration of model (5). We consider spatiotemporal evolution of this system with colored noise evolving in the time when the system lies within the regime of Turing space. We are interested in how noise affects the dynamics for fixed deterministic parameters and the extent to which noise is capable of changing the patterns exhibited by the deterministic system. Taking multiplicative colored noise into account, we consider the noise-induced patterns corresponding to the three typical types of patterns in the deterministic system.

Figure 8 shows the spatial patterns, which are corresponding to the H_π hexagon patterns, for different values of the noise intensity q and fixed temporal correlation τ_c. When there is no noise, the H_π hexagon patterns emerge. For the small value of noise intensity $q = 10^{-11}$, the H_π hexagon patterns are only slightly perturbed by the noise as depicted in Fig. 8(b), but the number of the patterns decreases. Increasing the noise intensity to $q = 10^{-9}$, the system transfers from the H_π hexagon patterns to the regular stripe patterns through the pattern transition. When the noise intensity is increased to

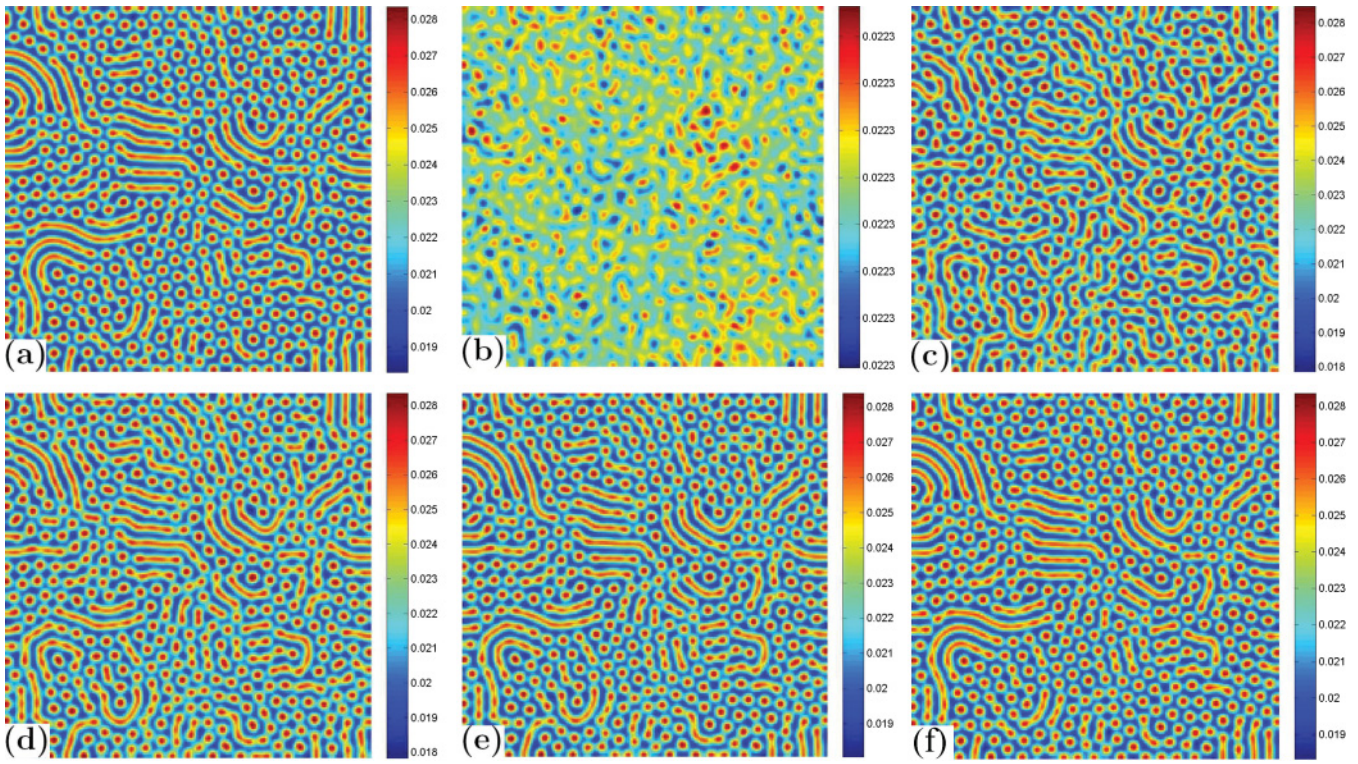

FIG. 5. (Color online) Snapshots of contour pictures of the time evolution of v at different instants with $\alpha = 0.095, \delta = 0.6, \gamma = 0.9, d_1 = 0.01, d_2 = 1, \beta = 0.075$ and the parameter values in the Turing space. (a) 0 iteration; (b) 10 000 iterations; (c) 100 000 iterations; (d) 200 000 iterations; (e) 300 000 iterations; (f) 400 000 iterations.

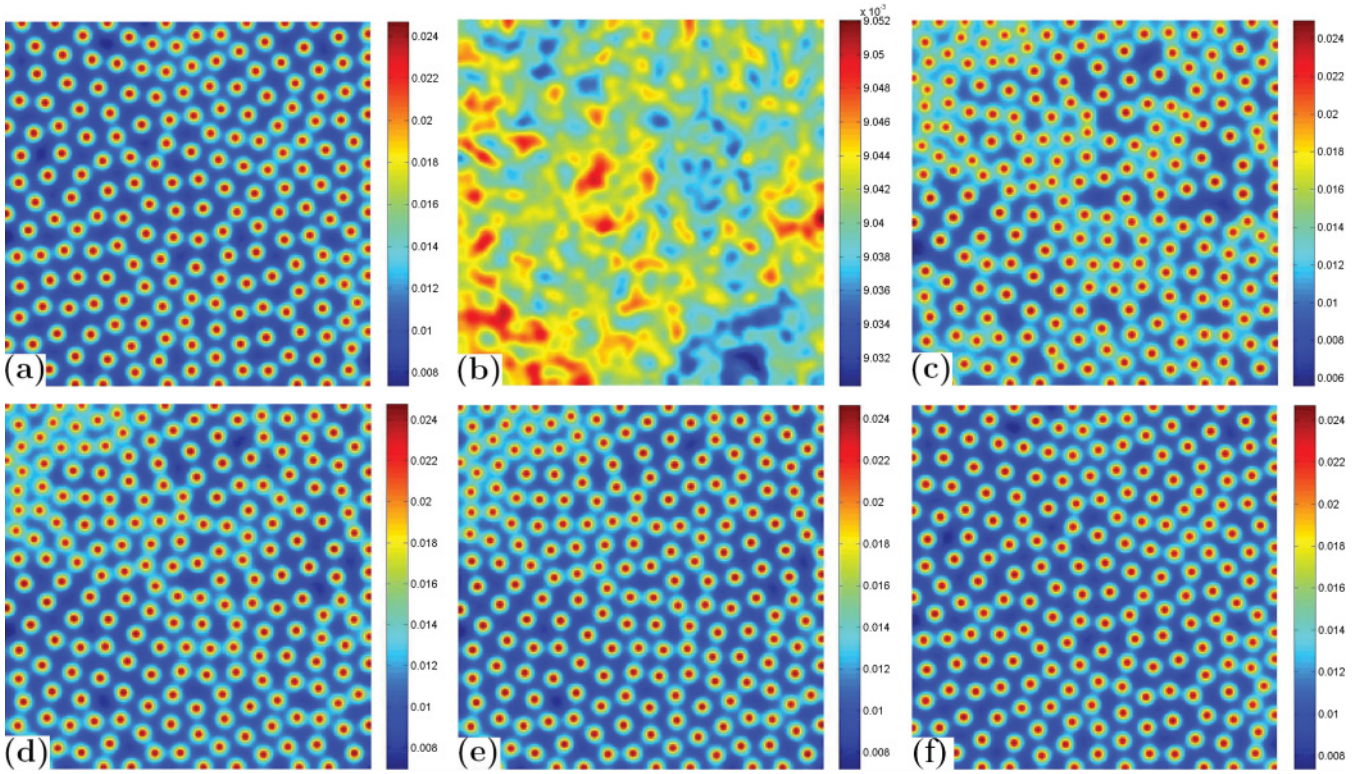

FIG. 6. (Color online) Snapshots of contour pictures of the time evolution of v at different instants with $\alpha = 0.095, \delta = 0.6, \gamma = 0.9, d_1 = 0.01, d_2 = 1, \beta = 0.025$ and the parameter values in the Turing space. (a) 0 iteration; (b) 10 000 iterations; (c) 100 000 iterations; (d) 200 000 iterations; (e) 300 000 iterations; (f) 400 000 iterations.

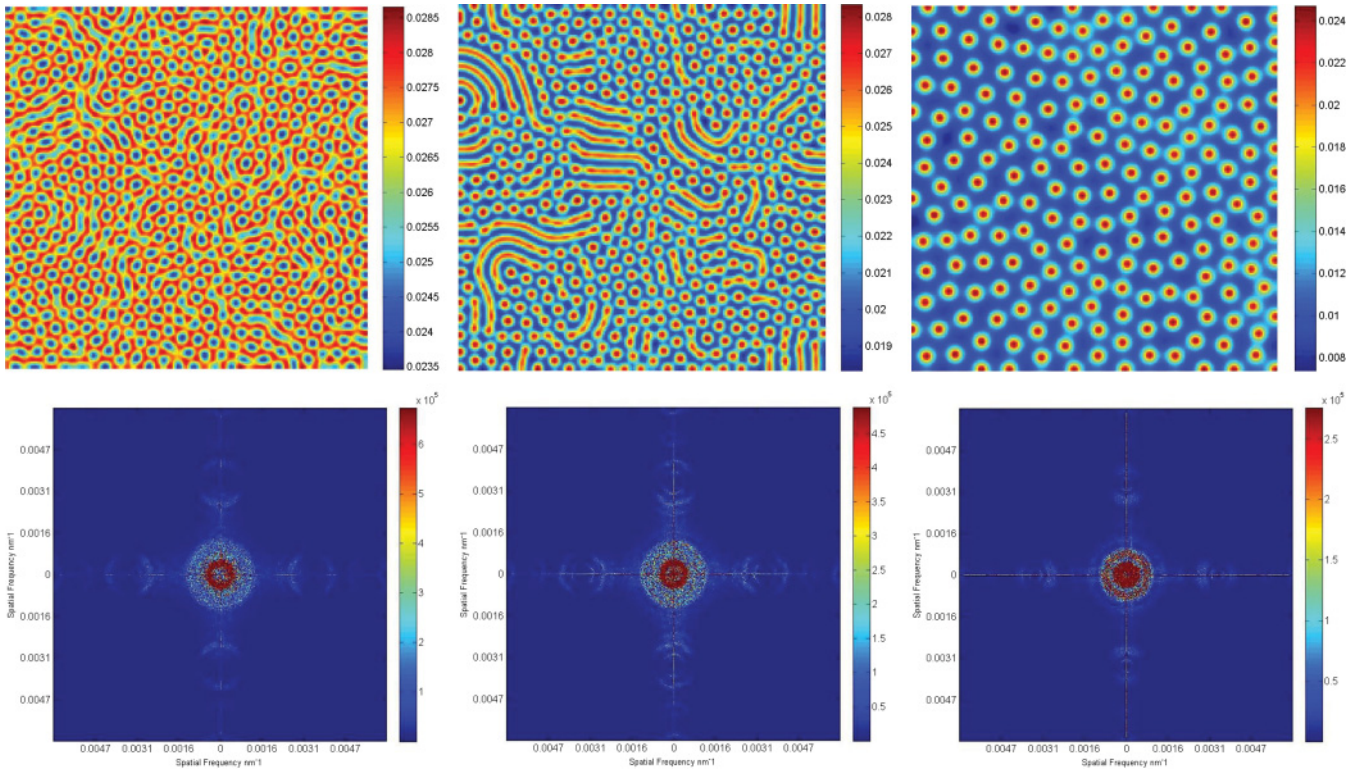

FIG. 7. (Color online) Stable Turing patterns that come from the numerical simulations of model (4) and their corresponding power spectrum. Left-hand row: $\beta = 0.098$; middle row: $\beta = 0.075$; right-hand row: $\beta = 0.025$.

$q = 10^{-7}$, there are only H_π hexagon patterns, but the H_π hexagon patterns are more regular. With regard to the pattern transition, we can give an intuitive explanation as follows. Noise can make the H_π hexagon patterns become bigger and bigger. As the increase of the noise intensity, the H_π hexagon patterns break up into stripe patterns gradually, and these stripe patterns join into regular stripe patterns eventually. When the noise intensity is increased to a certain extent, the stripe patterns break up into shorter stripe patterns, and these stripe patterns join into regular H_π hexagon patterns eventually.

Figure 9 shows the spatial patterns, which are corresponding to the coexistence of H_0 hexagon patterns and stripe patterns, for different values of the noise intensity q and fixed temporal correlation τ_c. When there is no noise, we notice the coexistence of H_0 hexagon patterns and stripe patterns. For the small value of noise intensity $q = 10^{-11}$, the H_π hexagon patterns remain nearly the same as depicted in Fig. 9(b), but the number of patterns decreases. Increasing the noise intensity to $q = 10^{-9}$, the stripe patterns dominate the domain eventually. When the noise intensity is increased to $q = 10^{-7}$, the system transfers from the coexistence of H_0 hexagon patterns and stripe patterns to the regular stripe patterns through the pattern transition. As described in Fig. 8, with the increase of the noise intensity, noise can make the H_0 hexagon patterns and stripe patterns become bigger and bigger, and the H_0 hexagon patterns and stripe patterns join into regular stripe patterns eventually. However, the stripe patterns do not break up into H_π hexagon patterns again.

Figure 10 shows the spatial patterns, which are corresponding to the H_0 hexagon patterns, for different values of the noise intensity q and fixed temporal correlation τ_c. When there is no noise, we discover the H_0 hexagon patterns. For different values of noise intensity $q = 10^{-11}$, $q = 10^{-9}$, and $q = 10^{-7}$, the H_0 hexagon patterns do not transfer to other types of patterns, but the number of the patterns decreases in each case, and the H_0 hexagon patterns become more and

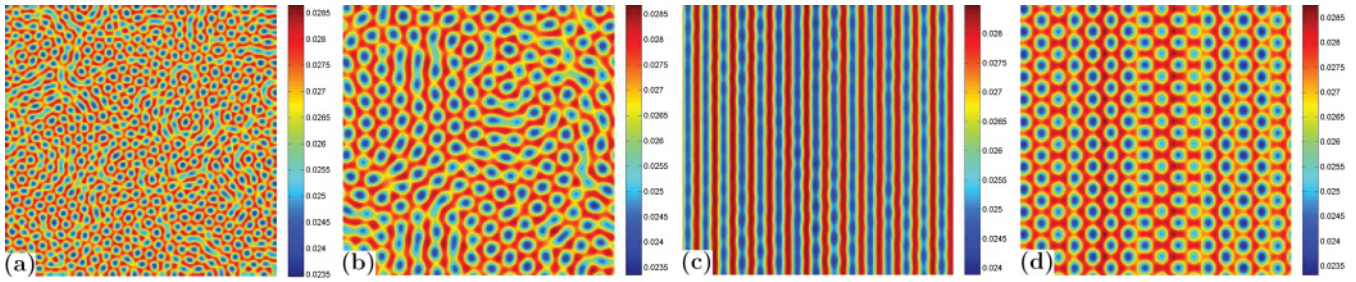

FIG. 8. (Color online) Snapshots of contour pictures of v as the value of noise intensity q being increased. Parameter values used: $\alpha = 0.095, \delta = 0.6, \gamma = 0.9, d_1 = 0.01, d_2 = 1, \beta = 0.098, \tau_c = 1$. (a) $q = 0$; (b) $q = 10^{-11}$; (c) $q = 10^{-9}$; (d) $q = 10^{-7}$.

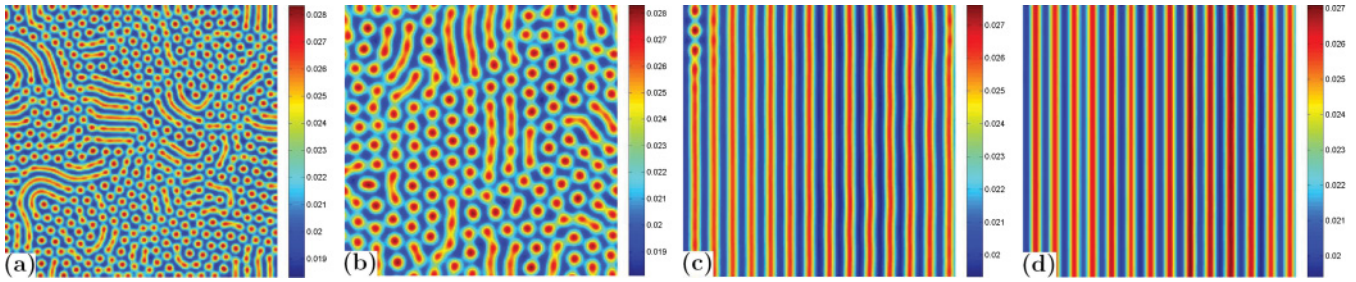

FIG. 9. (Color online) Snapshots of contour pictures of v as the value of noise intensity q being increased. Parameter values used: $\alpha = 0.095, \delta = 0.6, \gamma = 0.9, d_1 = 0.01, d_2 = 1, \beta = 0.075, \tau_c = 1$. (a) $q = 0$; (b) $q = 10^{-11}$; (c) $q = 10^{-9}$; (d) $q = 10^{-7}$.

more regular with the increase of the noise intensity. We can see that noise has less effect on the H_0 hexagon patterns. In other words, the H_0 hexagon patterns are more stable than the other two types of patterns. Similarly, noise can make the H_0 hexagon patterns bigger. But different from the H_π hexagon patterns, there is no pattern transition in this case. The H_0 hexagon patterns just become more regular eventually.

V. DISCUSSION AND CONCLUSIONS

This study presents the Turing pattern selection and noise-induced patterns in the Beddington-DeAngelis predator-prey model. For the model without noise, we find that the predator-prey model with a Beddington-DeAngelis functional response has rich dynamical behaviors. More specifically, in the range $\mu_2 < \mu < \mu_3$, H_π hexagon patterns emerge; in the range $\mu_3 < \mu < \mu_4$, there coexist H_0 hexagon patterns and stripe patterns; and in the range $\mu > \mu_4$, there appear H_0 hexagon patterns. In this study we find an interesting phenomenon that by increasing the systems's prey carrying capacity, i.e., decreasing the value of β, the density of the predators decreases gradually. This is called a "paradox of enrichment," which has been studied by some researchers [67,68]. However, in some previous work it is called the hypothesis of "the paradox of enrichment" [69–73]. For this reason, we consider the ecosystem as an open system to better describe the real ecosystem. Taking the environmental noise into account, we find that noise can decrease the number of the patterns and make the patterns more regular. What is more, noise can induce the typical pattern transitions from the H_π hexagon patterns to the regular stripe patterns and from the coexistence of H_0 hexagon patterns and stripe patterns to the regular stripe patterns. Another interesting result is that the H_0 hexagon patterns are more stable than the H_π hexagon patterns and the coexistence of H_0 hexagon patterns and stripe patterns. We also find that noise can change the density of the predators. In a word, noise can affect the pattern structures.

Neuhauser and Pacala [74] formulated the Lotka-Volterra model as a spatial model. They found the striking result that the coexistence of patterns is actually harder to obtain in the spatial model than in the nonspatial one. In this paper we obtain the coexistence of stationary stripe patterns and hexagon patterns. From the analysis and the numerical simulations in Sec. III, we find this study valuable in two aspects. First, it establishes the amplitude equations for the active modes, which determine the stability of the amplitudes toward uniform and inhomogeneous perturbations. Second, it illustrates different Turing patterns close to the onset of the Turing bifurcation line through numerical simulations, which indicate that the dynamics of the model exhibit complex pattern replication. At the same time, we find that when the system is not so close to the critical points μ_2 and μ_3, the numerical results cannot correspond perfectly to our theoretical analysis, which can be seen in Fig. 11. That is to say, our theoretical analysis is appropriate just for the adjacent domains of the critical points μ_2 and μ_3. When the system gets away from the critical points, the theoretical analysis is not so accurate. Through the patterns in this paper, we can find that the transition from H_π hexagon patterns to the coexistence of stripe patterns and H_0 hexagon patterns is a gradual progress. In the range $\mu_2 < \mu < \mu_3$, as μ moves away from μ_2; i.e., with the decrease of β, the H_π hexagon patterns break up into stripe patterns gradually, and these stripe patterns join into longer stripe patterns. When μ is very close to μ_3, there are nearly stripe patterns left. When μ exceeds μ_3, the stripe patterns break up into H_0 hexagon patterns gradually. Finally, there are only H_0 hexagon patterns left.

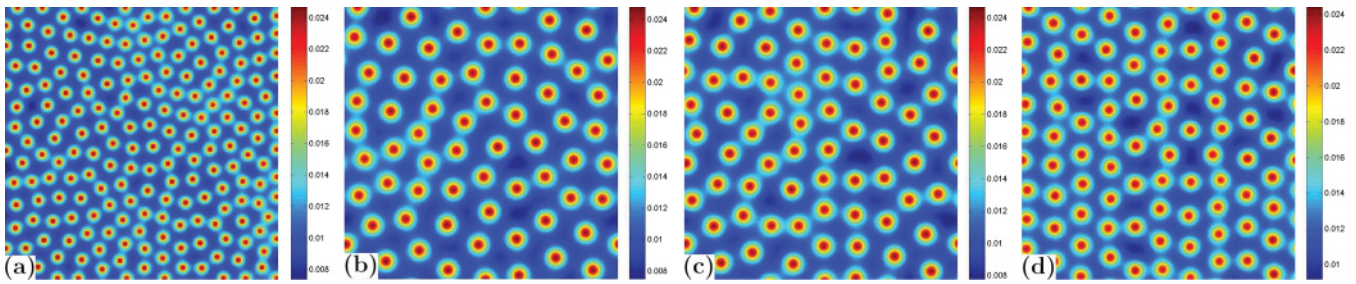

FIG. 10. (Color online) Snapshots of contour pictures of v as the value of noise intensity q being increased. Parameter values used: $\alpha = 0.095, \delta = 0.6, \gamma = 0.9, d_1 = 0.01, d_2 = 1, \beta = 0.025, \tau_c = 1$. (a) $q = 0$; (b) $q = 10^{-11}$; (c) $q = 10^{-9}$; (d) $q = 10^{-7}$.

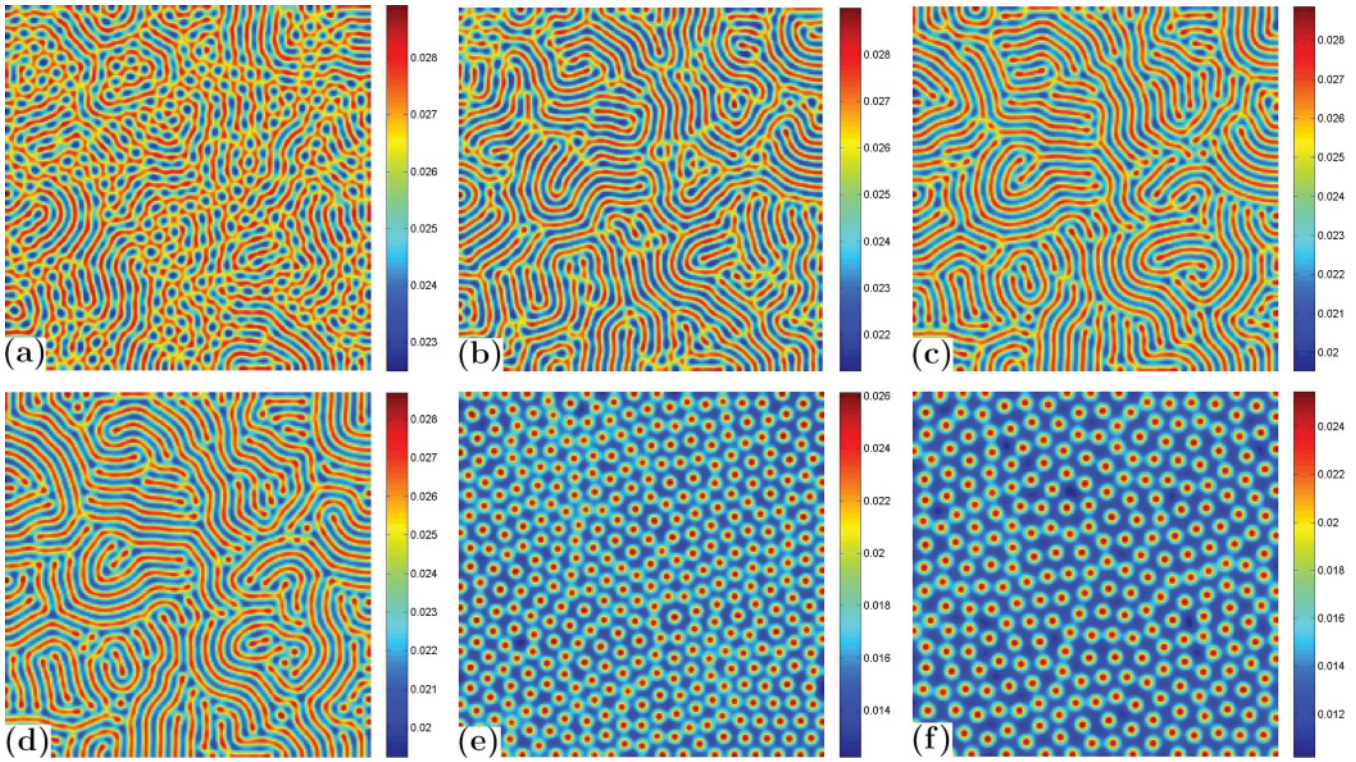

FIG. 11. (Color online) Snapshots of contour pictures of v and the parameter values in the Turing space. (a) $\beta = 0.095$, $\mu = 0.06638245874 \in (\mu_2,\mu_3)$; (b) $\beta = 0.09$, $\mu = 0.1155202241 \in (\mu_2,\mu_3)$; (c) $\beta = 0.085$, $\mu = 0.06638245874 \in (\mu_2,\mu_3)$; (d) $\beta = 0.083$, $\mu = 0.1155202241 \in (\mu_3,\mu_4)$; (e) $\beta = 0.045$, $\mu = 0.5577601126 \in (\mu_3,\mu_4)$; (f) $\beta = 0.035$, $\mu = 0.6560356433 \in (\mu_3,\mu_4)$.

ACKNOWLEDGMENTS

This work is supported by the National Natural Science Foundation of China under Grant Nos. 11171314 and 11147015, International and Technical Cooperation Project of Shan'xi Province (2010081005), Program for Basic Research of Shan'xi Province (2010011007), and Scientific Research Item for the Returned Overseas Chinese Scholars of Shan'xi Province.

APPENDIX A

Model (3) has a unique equilibrium (u^*,v^*) with $u^* > 0, v^* > 0$ if $0 < \beta < \frac{\gamma-\delta}{\delta}$. Moreover, (u^*,v^*) satisfies $|\mathbf{J}(u^*,v^*)| > 0$.

Proof. From the above, we know that α,β,γ, and δ are all positive constants. Obviously u^* is larger than zero. Since $v^* = (\frac{\gamma}{\delta} - 1)u^* - \beta$, $\gamma > \delta$ is the necessary condition for $v^* > 0$. Letting $v^* > 0$, we obtain $\beta < \frac{\gamma-\delta}{\delta}$. So $0 < \beta < \frac{\gamma-\delta}{\delta}$ ensures $v^* > 0$.

By $f(u^*,v^*) = g(u^*,v^*) = 0$, we have

$$\alpha(1-u^*)(\beta+u^*+v^*) = v^*, \quad \gamma u^* = \delta(\beta+u^*+v^*).$$

Equations (10) can be converted into the following form:

$$\begin{aligned} a_{11} &= -\frac{\alpha\gamma}{\delta}(u^*)^2 + \alpha u^*(1-u^*), \\ a_{12} &= \alpha u^*(1-u^*) - u^*, \\ a_{21} &= \gamma v^* - \delta v^*, \\ a_{22} &= -\delta v^*. \end{aligned}$$

Then we can have

$$\begin{aligned} |\mathbf{J}(u^*,v^*)| &= a_{11}a_{22} - a_{12}a_{21} \\ &= \alpha\gamma(u^*)^2v^* - \alpha\delta u^*v^*(1-u^*) - \alpha\gamma u^*v^*(1-u^*) \\ &\quad + \alpha\delta u^*v^*(1-u^*) + \gamma u^*v^* - \delta u^*v^* \\ &= u^*v^*[\alpha\gamma(2u^*-1) + \gamma - \delta] \\ &= u^*v^*\sqrt{(\alpha\gamma-\gamma+\delta)^2 + 4\alpha\gamma\delta\beta} > 0. \end{aligned}$$

APPENDIX B: THE PARAMETERS THAT ARE NOT EXPLAINED IN THE ABOVE

Substituting β_T for β in $a_{11}, a_{12}, a_{21}, a_{22}$, we obtain $a_{11}^*, a_{12}^*, a_{21}^*, a_{22}^*$. The expression of some parameters are as follows:

$$c = \sqrt{(\alpha\gamma-\gamma+\delta)^2 + 4\alpha\gamma\delta\beta_T}, \quad d = 1 - \left(\frac{\gamma}{\delta}+2\right)\frac{\alpha\gamma-\gamma+\delta+c}{2\alpha\gamma}, \quad e = \alpha - 1 - \frac{\alpha\gamma-\gamma+\delta+c}{\gamma},$$

$$l = \frac{a_{11}^*d_2 - a_{22}^*d_1}{2a_{21}^*d_1}, \quad b_{11} = -\frac{\delta}{c}\left(\frac{\gamma-\alpha*\gamma}{\delta} - \frac{\delta}{\gamma}\right) + 1 + \frac{\delta}{\gamma}, \quad b_{12} = \frac{\delta^2}{\gamma c} + \frac{\delta}{\gamma}, \quad b_{21} = -\frac{(\gamma-\delta)^2}{c} + \gamma - \delta,$$

$$b_{22}=\frac{\delta(\gamma-\delta)}{c}-\delta,\quad k_T^{*2}=\sqrt{\frac{a_{11}^*a_{22}^*-a_{12}^*a_{21}^*}{d_1d_2}},$$

$$x_0=\frac{1}{a_{11}^*a_{22}^*-a_{12}^*a_{21}^*}\left(a_{22}^*\left\{2\alpha l^2\left[1-\left(\frac{\gamma}{\delta}+2\right)\frac{\alpha\gamma-\gamma+\delta+c}{2\alpha\gamma}\right]+2l\left(\alpha-1-\frac{\alpha\gamma-\gamma+\delta+c}{\gamma}\right)\right\}-a_{12}^*[2l(\gamma-\delta)-2\delta]\right),$$

$$y_0=\frac{1}{a_{11}^*a_{22}^*-a_{12}^*a_{21}^*}\left(-a_{21}^*\left\{2\alpha l^2\left[1-\left(\frac{\gamma}{\delta}+2\right)\frac{\alpha\gamma-\gamma+\delta+c}{2\alpha\gamma}\right]+2l\left(\alpha-1-\frac{\alpha\gamma-\gamma+\delta+c}{\gamma}\right)\right\}+a_{11}^*\left[2l(\gamma-\delta)-2\delta\right]\right),$$

$$x_{11}=\frac{1}{(a_{11}^*-4d_1k_T^{*2})(a_{22}^*-4d_2k_T^{*2})-a_{12}^*a_{21}^*}\left(\left\{\left(a_{22}^*-4d_2k_T^{*2}\right)\left(\alpha l^2\left[1-\left(\frac{\gamma}{\delta}+2\right)\frac{\alpha\gamma-\gamma+\delta+c}{2\alpha\gamma}\right]\right.\right.$$
$$\left.\left.+l\left(\alpha-1-\frac{\alpha\gamma-\gamma+\delta+c}{\gamma}\right)\right\}-a_{12}^*[l(\gamma-\delta)-\delta]\right),$$

$$y_{11}=\frac{1}{(a_{11}^*-4d_1k_T^{*2})(a_{22}^*-4d_2k_T^{*2})-a_{12}^*a_{21}^*}\left(-a_{21}^*\left\{\alpha l^2\left[1-\left(\frac{\gamma}{\delta}+2\right)\frac{\alpha\gamma-\gamma+\delta+c}{2\alpha\gamma}\right]+l\left(\alpha-1-\frac{\alpha\gamma-\gamma+\delta+c}{\gamma}\right)\right\}\right.$$
$$\left.+(a_{11}^*-4d_1k_T^{*2})[l(\gamma-\delta)-\delta]\right),$$

$$x^*=\frac{1}{(a_{11}^*-3d_1k_T^{*2})(a_{22}^*-3d_2k_T^{*2})-a_{12}^*a_{21}^*}\left(\left(a_{22}^*-3d_2k_T^{*2}\right)\left\{2\alpha l^2\left[1-\left(\frac{\gamma}{\delta}+2\right)\frac{\alpha\gamma-\gamma+\delta+c}{2\alpha\gamma}\right]\right.\right.$$
$$\left.\left.+2l\left(\alpha-1-\frac{\alpha\gamma-\gamma+\delta+c}{\gamma}\right)\right\}-a_{12}^*[2l(\gamma-\delta)-2\delta]\right),$$

$$y^*=\frac{1}{(a_{11}^*-3d_1k_T^{*2})(a_{22}^*-3d_2k_T^{*2})-a_{12}^*a_{21}^*}\left(-a_{21}^*\left\{2\alpha l^2\left[1-\left(\frac{\gamma}{\delta}+2\right)\frac{\alpha\gamma-\gamma+\delta+c}{2\alpha\gamma}\right]\right.\right.$$
$$\left.\left.+2l\left(\alpha-1-\frac{\alpha\gamma-\gamma+\delta+c}{\gamma}\right)\right\}+(a_{11}^*-3d_1k_T^{*2})[2l(\gamma-\delta)-2\delta]\right),$$

$$G_1=\frac{d_1}{d_2}l\{(\gamma-\delta)[l(y_{11}+y_0)+x_{11}+x_0]-2\delta(y_{11}+y_0)\}-[2\alpha dl(x_{11}+x_0)+el(y_{11}+y_0)+e(x_{11}+x_0)-3\alpha l^2-3\alpha l^3],$$

$$G_2=\frac{d_1}{d_2}l\{(\gamma-\delta)[l(y^*+y_0)+x^*+x_0]-2\delta(y^*+y_0)\}-[2\alpha dl(x^*+x_0)+el(y^*+y_0)+e(x^*+x_0)-6\alpha l^2-6\alpha l^3],$$

$$\tau_0=\frac{(d_2-d_1)l}{\beta_T d_2\left[lb_{11}+b_{12}-\frac{d_1}{d_2}l(lb_{21}+b_{22})\right]},\quad h=\frac{\left\{2\alpha dl+2e-\frac{d_1}{d_2}[2l(\gamma-\delta)-2\delta]\right\}l}{\beta_T\left[lb_{11}+b_{12}-\frac{d_1}{d_2}l(lb_{21}+b_{22})\right]},$$

$$g_1=\frac{G_1}{\beta_T\left[lb_{11}+b_{12}-\frac{d_1}{d_2}l(lb_{21}+b_{22})\right]},\quad g_2=\frac{G_2}{\beta_T\left[lb_{11}+b_{12}-\frac{d_1}{d_2}l(lb_{21}+b_{22})\right]}.$$

[1] J. R. Beddington, J. Animal Ecol. **44**, 331 (1975).
[2] D. L. DeAngelis, R. A. Goldstein, and R. V. O'Neill, Ecology **56**, 881 (1975).
[3] G. T. Skalski and J. F. Gilliam, Ecology **82**, 3083 (2001).
[4] M. P. Hassell and C. C. Varley, Nature (London) **223**, 1133 (1969).
[5] P. H. Crowley and E. K. Martin, J. N. Am. Benthol. Soc. **8**, 211 (1989).
[6] A. M. Turing, Philos. Trans. R. Soc. London B **237**, 37 (1952).
[7] M. P. Hassell, H. N. Comins, and R. M. May, Nature (London) **353**, 255 (1991).
[8] Q. Ouyang and H. L. Swinney, Nature (London) **352**, 610 (1991).
[9] J. D. Murray, *Mathematical Biology 19* (Springer-Verlag, Berlin, London, 1993).
[10] V. Dufiet and J. Boissonade, Phys. Rev. E **53**, 4883 (1996).
[11] C. Varea, J. L. Aragon, and R. A. Barrio, Phys. Rev. E **56**, 1250 (1997).
[12] S. Kondo and R. Asai, Nature (London) **376**, 765 (1995).
[13] W. S. C. Gurney, A. R. Veitch, I. Cruickshank, and G. McGeachin, Ecology **79**, 2516 (1998).
[14] L. Saunoriene and M. Ragulskis, Phys. Rev. E **84**, 056213 (2011)
[15] T. E. Woolley, R. E. Baker, E. A. Gaffney, and P. K. Maini, Phys. Rev. E **84**, 046216 (2011).
[16] V. N. Biktashev and M. A. Tsyganov, Phys. Rev. Lett. **107**, 134101 (2011).
[17] L. Segel and J. Jackson, J. Theor. Biol. **37**, 545 (1972).
[18] A. Gierer and H. Meinhardt, Kybernetik **12**, 30 (1972).
[19] S. Levin and L. Segel, Nature (London) **259**, 659 (1976).
[20] G.-Q. Sun, Z. Jin, Q.-X. Liu, and L. Li, Ecol. Model. **219**, 248 (2008).
[21] G.-Q. Sun, Z. Jin, Q.-X. Liu, and L. Li, Chin. Phys. B **17**, 3936 (2008).
[22] G.-Q. Sun, G. Zhang, Z. Jin, and L. Li, Nonlinear Dynam. **58**, 75 (2009).

[23] G.-Q. Sun, Z. Jin, L. Li, and B.-L. Li, Nonlinear Dynam. **60**, 265 (2010).
[24] A. Sengupta, T. Kruppa, and H. Lowen, Phys. Rev. E **83**, 031914 (2011).
[25] Y.-M. Lai, J. Newby, and P. C. Bressloff, Phys. Rev. Lett. **107**, 118102 (2011).
[26] T. Callahan and E. Knobloch, Physica D **132**, 339 (1999).
[27] G. H. Gunaratne, Q. Ouyang, and H. L. Swinney, Phys. Rev. E **50**, 2802 (1994).
[28] M. Ipsen, F. Hynne, and P. Søensen, Physica D **136**, 66 (2000).
[29] B. Peña and C. Pérez-García, Phys. Rev. E **64**, 056213 (2001).
[30] P. Manneville, *Dissipative Structures and Weak Turbulence* (Academic Press, San Diego, 2000).
[31] B. Spagnolo and A. La Barbera, Physica A **315**, 114 (2002).
[32] F. N. Braun, T. J. Sluckin, E. Velasco, and L. Mederos, Phys. Rev. E **53**, 706 (1996).
[33] A. La Cognata, D. Valenti, A. A. Dubkov, and B. Spagnolo, Phys. Rev. E **82**, 011121 (2010).
[34] L. Gammaitoni, P. Hänggi, P. Jung, and F. Marchesoni, Rev. Mod. Phys. **70**, 223 (1998).
[35] R. N. Mantegna, B. Spagnolo, and M. Trapanese, Phys. Rev. E **63**, 011101 (2000).
[36] B. Spagnolo, D. Valenti, and A. Fiasconaro, Math. Biosci. Eng. **1**, 185 (2004).
[37] B. Spagnolo, A. A. Dubkov, and N. V. Agudov, Eur. Phys. J. B **40**, 273 (2004).
[38] N. V. Agudov and B. Spagnolo, Phys. Rev. E **64**, 035102(R) (2001).
[39] B. Spagnolo, A. Fiasconaro, and D. Valenti, Fluct. Noise Lett. **3**, L177 (2003).
[40] D. Valenti, A. Fiasconaro, and B. Spagnolo, Physica A **331**, 477 (2004).
[41] C. R. Doering and J. C. Gadoua, Phys. Rev. Lett. **69**, 2318 (1992).
[42] J. Iwaniszewski, Phys. Rev. E **68**, 027105 (2003).
[43] C. VandenBroeck, J. M. R. Parrondo, and R. Toral, Phys. Rev. Lett. **73**, 3395 (1994).
[44] G.-Q. Sun, Z. Jin, Q.-X. Liu, and B.-L. Li, BioSystems **100**, 14 (2010).
[45] D. Valenti, A. Fiasconaro, and B. Spagnolo, Acta Phys. Pol. B **35**, 1481 (2004).
[46] A. Fiasconaro, D. Valenti, and B. Spagnolo, Fluct. Noise Lett. **5**, L305 (2005).
[47] M. Haque, Math. Biosci. **234**, 1 (2011).
[48] M. Haque, Bull. Math. Biol. **71**, 430 (2009).
[49] M. Zhao and S. J. Lv, Chaos Solitons Fractals **40**, 2305 (2009).
[50] H. K. Baek, Nonlinear Anal.-REAL **11**, 1312 (2010).
[51] X. Zhang, Q.-L. Zhang, and V. Sreeramb, J. Franklin Inst. **347**, 1076 (2010).
[52] H.-Y. Li and Y. Takeuchi, J. Math. Anal. Appl. **374**, 644 (2011).
[53] H.-J. Guo and X.-X. Chen, Appl. Math. Comput. **217**, 5830 (2011).
[54] Y. Tang and W. Zhang, J. Math. Biol. **50**, 669 (2005).
[55] F. Berezovskaya, G. Karev, and R. Arditi, J. Math. Biol. **43**, 221 (2001).
[56] B. Li and Y. Kuang, SIAM J. Appl. Math. **67**, 1453 (2007).
[57] A. Fiasconaro, D. Valenti, and B. Spagnolo, Acta Phys. Pol. B **35**, 1491 (2004).
[58] H. Wang, K. Zhang, and Q. Ouyang, Phys. Rev. E **74**, 036210 (2006).
[59] P. Arcuri and J. D. Murray, J. Math. Biol. **24**, 141 (1986).
[60] M. C. Cross and P. C. Hohenberg, Rev. Mod. Phys. **65**, 851 (1993).
[61] W. Wang, Q.-X. Liu, and Z. Jin, Phys. Rev. E **75**, 051913 (2007).
[62] T. Leppänen, Ph.D. Thesis, Helsinki University of Technology, Finland, 2004.
[63] L. Yang, M. Dolnik, A. Zhabotinsky, and I. Epstein, J. Chem. Phys. **117**, 7259 (2002).
[64] V. Dufiet and J. Boissonade, Phys. Rev. E **53**, 4883 (1996).
[65] Q. Ouyang, *Pattern Formation in Reaction-Diffusion Systems* (Shanghai Sci-Tech Education Publishing House, Shanghai, 2000).
[66] O. JenSen, V. O. Pannbacker, G. Dewel, and P. Borckmans, Phys. Lett. A **179**, 91 (1993).
[67] C. Huffaker, S. Herman, and K. Shea, Experimental studies on predation: complex dispersion and levels of food in an acarine predator-prey interaction, Univ. of Calif. (1963), [http://books.google.com.hk/books?id=7y5ZMwAACAAJ].
[68] B. V. Shea, J. Anim. Ecol. **48**, 787 (1979).
[69] M. Vos and B. W. Koori, Oikos **105**, 471 (2004).
[70] M. Vos, A. M. Verschoor, B. W. Koori, D. L. Wackers, D. L. DeAngelis, and W. M. Mooij, Ecology **85**, 2783 (2004).
[71] E. McCauley and W. W. Murdoch, Nature (London) **343**, 455 (1990).
[72] A. Persson, L. A. Hansson, C. Broenmark, P. Lundberg, L. B. Pettersson, L. Greenberg, P. A. Nilsson, P. Nystrom, P. Romare, and L. Tranvik, Am. Nat. **157**, 654 (2001).
[73] K. L. Kirk, Ecology **79**, 2456 (1998).
[74] C. Neuhauser and S. W. Pacala, Ann. Appl. Prob. **9**, 1226 (1999).